Time-resolved stereo PIV investigation of the NASA Common Research Model in the NASA Ames Fluid Mechanics Laboratory 32- by 48-in indraft wind tunnel

By Đ. S. Čantrak†, L. K. Kushner‡ AND J. T. Heineck¶

1. Motivation and objectives

The NASA Common Research Model (CRM) was developed as an open-source contemporary transonic supercritical wing for various studies in aerodynamics (Vassberg *et al.* (2008)). Extensive detailed aerodynamic performance data have been generated since 2008, and collection of such data is still under way. These data serve as a good basis for CFD studies generally and, in particular, for the research presented in this paper.

Rivers & Dittberner (2011) presented results of the experimental aerodynamics investigations of the CRM conducted in the NASA Langley National Transonic Facility (NTF) and the 11- by 11-ft Transonic Wind Tunnel (11x11 TWT). The same model was tested in both wind tunnels at chord Reynolds numbers of $5 \cdot 10^6$ for five different configurations. Force, moment, surface pressure, and surface flow visualization data were obtained. Nacelle/pylon and tail effects, as well as the influence of the sting mounting systems were investigated.

Rivers & Hunter (2012) investigated wing-body-tail configurations at angle of attack 0° with and without the support system. They concluded that the support system must be added to the computational case for better simulation results. Acheson & Balakrishna (2011) and Rivers *et al.* (2012) also reported the effect of sting damping on CRM data quality.

Zilliac *et al.* (2011) measured the skin friction distribution on the CRM at transonic conditions in the 11x11 TWT using the Fringe Imaging Skin Friction (FISF) technique. These measurements were compared with Reynolds-Averaged Navier Stokes (RANS) solutions and the differences were analyzed. Bell (2011) presented pressure-sensitive paint (PSP) measurements on a 2.7% CRM in the 11x11 TWT. PSP data were obtained at three transonic Mach numbers (M=0.7, 0.85, and 0.87) and nine angles of attack.

Experimental data from both the NTF and 11x11 TWT consist of force and moment, skin friction, surface pressures, and wideband wing-root dynamic strain wing Kulite pressure sensor data. Balakrishna & Acheson (2011) analyzed the dynamic data sets, acquired at a sampling rate of 12.8 kHz with the aim: "... to evaluate CRM wing buffet onset and potential CRM wing flow separation ...".

CRM experiments are also planned in the European Transonic Wind Tunnel. Illi *et al.* (2013) used the DLR TAU code to compute the interaction between the separated flow of the wing with the horizontal tail plane at high Mach numbers (transonic tail buffet).

A wing tip vortex, a circulatory three-dimensional motion that trails downstream from

† University of Belgrade, Faculty of Mechanical Engineering, Serbia
‡ Aerospace Computing Inc.
¶ NASA Ames Research Center, Experimental Aero-Physics Branch

the wing, occurs as a result of pressure differences on the wing. The study of wing tip vortices has both engineering and scientific importance. These vortices are hazardous for airplanes in the take-off and landing phases of flight and for how quickly they diminish directly influences airport capacity. It is also a source of induced drag and can impact helicopter and smaller aircraft performance. Predicting wing tip vortices is still challenging for CFD codes due to the presence of significant velocity and pressure gradients at high Reynolds numbers. Numerous efforts have been made to study of the formation and decay process of the wing tip vortex, as well the ways to control it (Spalart (1998)).

Sohn & Chang (2012) studied wing tip vortices of a half-wing model for three different wing configurations by use of stereo particle image velocimetry (SPIV). Igarashi *et al.* (2010) reported on a SPIV experimental investigation of the wing tip vortex generated from a rectangular NACA0012 airfoil model.

This paper presents high-speed stereo particle image velocimetry (HSS PIV) measurements of the wing-tip vortex from a 3% scaled semi-span model of the CRM without nacelle or pylon. The measurements were made at three angles of attack in the 32- by 48-in indraft wind tunnel in the Fluid Mechanics Laboratory at NASA Ames.

2. Experimental setup

2.1. *Facility description*

The 32- by 48-in indraft wind tunnel is located in the Fluid Mechanics Laboratory (FML) at NASA Ames Research Center. The flow in this tunnel has a maximum velocity of 170 fps or approximately 51.8 m/s, and a freestream turbulence level of 0.15%. The tunnel test section is 10 ft long, 4 ft wide, and 32 in high. The test section is enclosed on two sides by hinged clear plexiglas panels to allow observation of objects inside. A wide range of flow measurement sensors and traversing gear can be mounted in an enclosed plenum located above the test section. The tunnel is driven by an Allis Chalmers single-stage centrifugal flow compressor with a Hitachi 9000 hp drive motor, Hitachi speed increasing gear, and a lubrication system. Data such as temperature, relative humidity, atmospheric pressure, and tunnel speed are measured and analyzed while the tunnel is on-line. A choked nozzle downstream of the test section prevents disturbances in the diffuser from propagating upstream into the test section. Figure 1 shows the Common Research Model placed in the test section.

The CRM model was installed on the north wall of the wind tunnel with a mechanism that allowed the angle of attack (α) to be changed. The CRM dimensions are specified in Figure 2.

The height of the wing tip trailing edge from the test section bottom was regularly checked while changing the angle of attack. The height was 16 3/16 in or 411.2 mm for the angle of attack $\alpha = 2°$, 15 1/2 in or 393.7 mm for the angle $\alpha = 4°$ and 16 13/16 in or 427.1 mm for the angle $\alpha = 0°$. It is accepted that only this dimension changes.

Wing trip dots (0.0114 in at 0.1 in spacing) were installed at 10% of the chord away from the leading edge to induce transition and reduce the possibility of separation and sensitivity to incoming flow, i.e., free-stream conditions. The wind tunnel speed was approximately the same for all measurements, but more precisely averaged 163.71 fps (or approximately 49.9 m/s) for angle of attack 2°, 164.54 fps (or app. 50.2 m/s) for angle 4° and for the last measurement 163.85 fps (or approximately 49.9 m/s) for angle 0°. This corresponds to a chord Reynolds number of $Re_C \approx 2.68 \cdot 10^5$, where the chord length of 3.2" is considered the characteristic length.

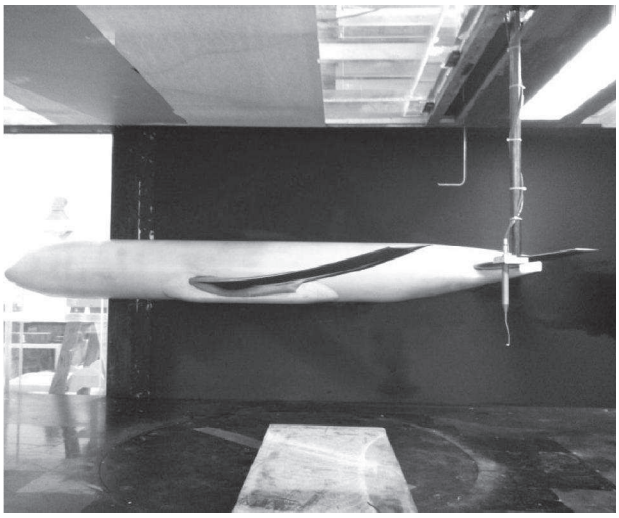

FIGURE 1. Common Research Model (CRM), 3% scaled semi-span, in FML 32- by 48-in indraft wind tunnel test section.

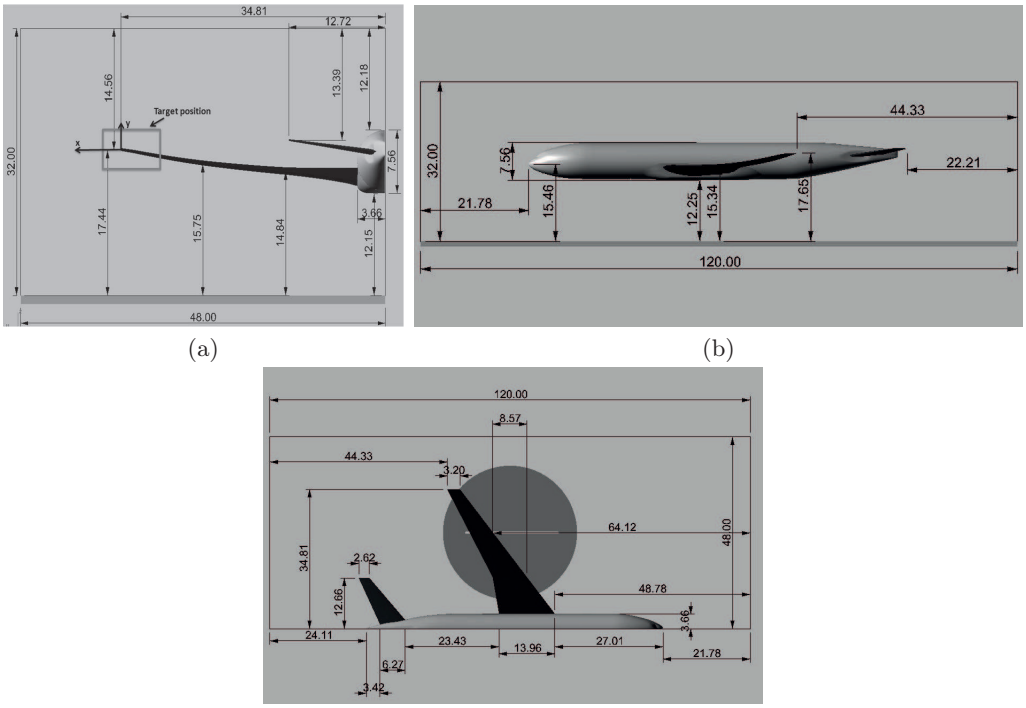

FIGURE 2. CRM dimensions at test section for angle of attack 0°: a) view from behind, b) side view, and c) top view. All dimensions are in inches.

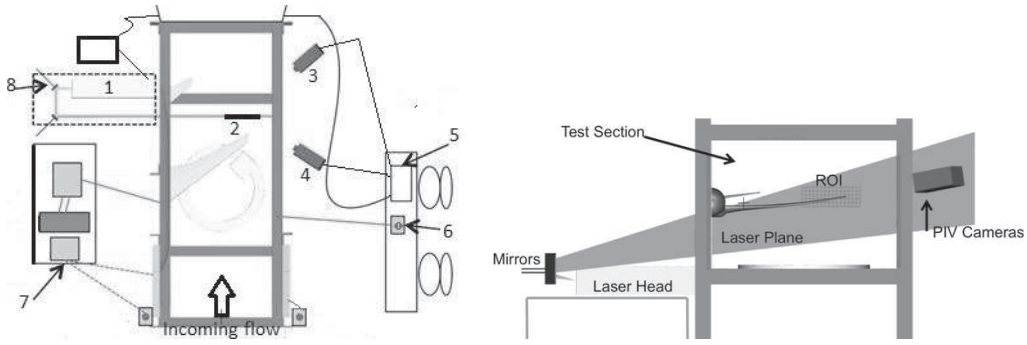

(a) (b)

FIGURE 3. Schematic of the experimental setup: a) stereo PIV diagram: 1, laser head; 2, test section; 3 & 4, CMOS cameras; 5, laser timing and data acquisition; 6, beam dump and emergency-stop switches; 7, laser safety system; and 8, turning mirrors and optics; b) top view of SPIV system and test section.

2.2. *Stereo PIV equipment*

A schematic of the experimental setup is shown in Figure 3. Fluid flow illumination was provided by a double-pulsed Nd:YLF laser (Quantronix Darwin-Duo) at 527 nm. Its average power at 3 kHz is greater than 100 W. It was pulsed at 2 kHz with pulse spacing on the orders of 10 μs. The laser beam was shaped to a sheet by spherical and cylindrical lenses and directed to the region of interest (ROI) (Figure 3(b)) by a set of mirrors. The laser sheet thickness in the ROI is approximately 1 mm.

Measurements were taken in a vertical cross-stream plane three tip-chords downstream of the wing tip trailing edge, i.e., 9.6 in, which corresponds to the origin of the coordinate system. The system was calibrated for $\alpha = 2°$. The coordinate system is presented in Figure 2(a). The third z-axis is directed downstream with the fluid flow.

Camera and laser positions were optimized using test-planning visualization software (Figure 3; Schairer *et al.* (2005)). The cameras viewed the ROI in forward scatter from opposite sides of the laser sheet. Limited optical access within the test section necessitated the use of Scheimpflug camera mounts for the stereo arrangement (Figure 3), as well as the use of custom wooden sidewalls for the tunnel which were inset with optical quality glass. Two high-speed 12-bit (full image size: 2560 x 1600 pixels) CMOS cameras, Phantom v641s, were used. The cameras were windowed to 1600 x 700 pixels at 4 kHz. For each run, 2088 image pairs per camera were recorded. Ten runs were performed per each angle of attack. The two CMOS cameras were positioned to obtain a wide view. Maximum dimensions of the ROI were x = 220 mm and y = 90 mm. Image acquisition and the laser timing were controlled with a LaVision controller and computer. The flow was seeded with 0.7-1 μm oil droplets that were injected through an array of pipes just upstream of the tunnel inlet.

Calibration data acquisition and data processing were performed using DaVis by La Vision. An in-situ calibration procedure generated a fourth-order multi-dimensional polynomial mapping function for the x- and y-directions in the laser sheet plane, and the second-order polynomial for the z-axis. The mapping function was determined by imaging a double-sided calibration plate and the self-calibration procedure in DaVis. In DaVis only time-averaged velocity components (V_i, where i = x, y, and z) are determined for all ten data sets for the three angles of attack. Vorticity is calculated afterwards on the

basis of time-averaged velocity fields also in DaVis. The total velocity calculation and data presentation were in Tecplot. Invariant maps and turbulent kinetic energy are determined by in-house software code TurbView made at the University of Belgrade, by Novica Janković and Đorđe Čantrak. Data processing was performed in multiple steps. Stereo cross-correlation was applied, using multi-pass iterations with decreasing the size of the interrogation window from 96 x 96 pixels in one pass and 50% overlap down to three passes with a final window size 32 x 32 pixels and 75% overlap. Median filtering was applied, as well as smoothing at a windows size of 3 x 3 pixels. Missing vectors were interpolated. All three velocity components were reconstructed in the ROI in this way. Each data run generated 17661 points with a 1.111 mm step in the x-axis direction and approximately the same in the y-direction (1.115). From the measured instantaneous velocity fields time-averaged quantities such as mean velocities (V_i, where i = x, y, and z), velocity fluctuations (v_i, where i = x, y, and z), turbulent kinetic energy, shear stresses and averaged vorticity (Ω_i, where i = x, y, and z) were derived.

3. Results and discussion

3.1. *Velocity and vorticity fields*

The tip vortex roll up from the trailed vorticity street is presented in Figures 4-11.

One data set is comprised of 2088 image pairs for each camera and together they generate the three-component velocity field (V_x, V_y, and V_z). Figure 4 shows the velocity fields for $\alpha = 0°$. Figure 4(a) presents one of these components - time-averaged axial velocity (V_z). The data set spans 1.044 s. Figure 4(b) shows ensemble averaged axial velocity ($V_{z,e}$) on the basis of ten data sets, or 20,880 image pairs. Data sets are completely independent, i.e., stochastic. This flow can clearly be treated as statistically stationary. Axial velocity is in accordance with the tunnel velocity. Vortex core position ($x \approx 0$ mm and $y \approx 15.5$ mm) corresponds to the trailing edge point at the wing tip, only three chords upstream. The wing tip vortex circulates counterclockwise (as viewed from downstream), the opposite direction from that of a wing creating positive lift. At the two higher angles the direction of circulation reversed and was consistent with a lifting wing. The total velocity minimum criterion for defining the vortex core was used as shown in Čantrak *et al.* (2014).

Ensemble-averaged velocities V_x and V_y are presented in Figures 4(c,d), respectively. Both cross-stream components have small values comparing to that of the dominant axial velocity. The vortex core is where the cross-stream velocities change sign and where the gradients are largest.

Total velocity on the basis of only one data set (V) is shown in Figure 5(a), while total ensemble velocity (V_e) obtained on the basis of ensemble averaged velocity components ($V_{x,e}$, $V_{y,e}$, and $V_{z,e}$) is shown in Figure 5(b).

These diagrams also show that this flow can be treated as statistically stationary. The vortex core position is also repeated here.

Velocity fields for $\alpha = 2°$ are presented in Figure 6. Flow can again be treated as statistically stationary. The vortex core, positioned at the end of the vorticity sheet, is at point ($x \approx -5.4$ mm and y = 14 mm) as read from the Tecplot diagram.

Looking upstream, the wing tip vortex in this case trails from the left-hand wing and circulates clockwise, as expected for a lifting wing. In this case, the downwash region behind the aircraft is generated. The vortex decays slowly, as shown in these measurements from three tip-chords downstream of the wingtip. The other two components of velocity

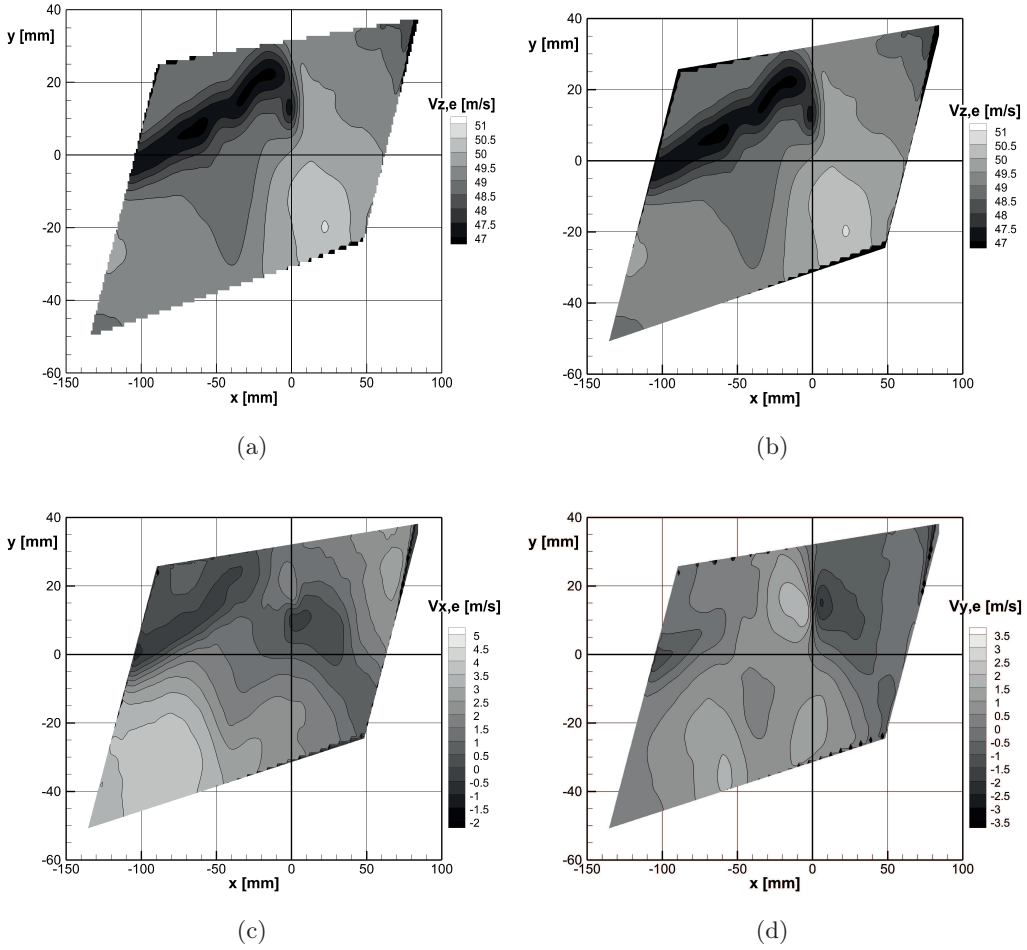

FIGURE 4. Velocity fields for $\alpha = 0°$: a) V_z, b) ensemble-averaged velocity V_z ($V_{z,e}$), c) ensemble-averaged velocity V_x ($V_{x,e}$), and d) ensemble-averaged velocity V_y ($V_{y,e}$).

(V_x and V_y) have similar intensities as for $\alpha = 0°$.

Velocity fields for the angle of attack 4° are shown Figure 7. The time-averaged total velocity minimum on the basis of just one experiment realization is V = 45.5 m/s (Figure 7(a)) in point x = -11.7 mm and y ≈ -1 mm, as read from the Tecplot diagram, while the ensemble-averaged velocity minimum is $V_e \approx 46$ m/s in the close point x = -11.8 mm and y = -2.2 mm (Figure 7(b)), which is again not aligned with the wing tip profile end point. Flow can again be treated as statistically stationary. The other two components (V_x and V_y) have intensities similar to those for the $\alpha = 0°$.

Streamwise vorticity ($\Omega_{z,a}$) for one data set, i.e., one experimental realization, calculated on the basis of the time-averaged velocity field, is shown in Figure 8(a). The average of ten vorticity fields ($\Omega_{z,10}$), obtained from ten averaged vorticity fields, is shown in Fig-

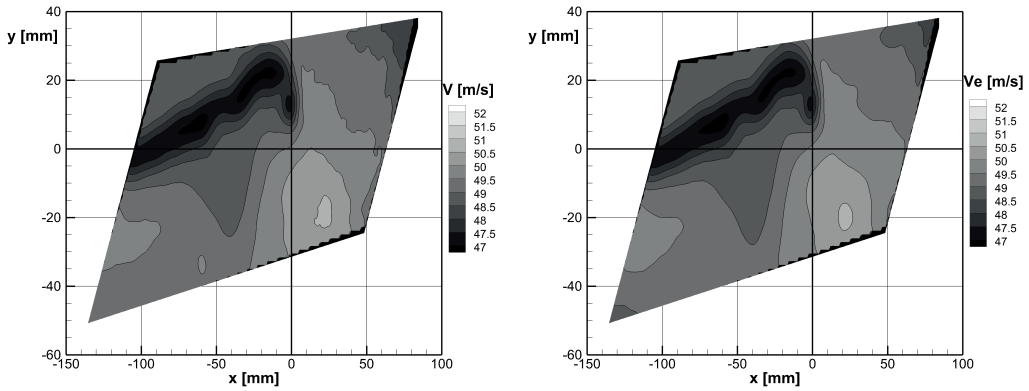

(a) (b)

FIGURE 5. Total velocity fields for the angle of attack $\alpha = 0°$: a) averaged total velocity (V) and b) ensemble-averaged total velocity (V_e).

ure 8(b). Maximum vorticity is obtained at the vortex core. This value occurs in approximately the same position as the total velocity minimum. High vorticities are obtained in the vorticity sheet region. Figure 9 shows averaged streamwise vorticities ($\Omega_{z,10}$) for $\alpha = 0°$ and 4°, respectively, obtained in the same way as in the case for $\alpha = 0°$.

The maximum streamwise vorticities are obtained in the same points as where total velocity minima occur. The highest streamwise vorticity ($\Omega_{z,10} \approx 8085\ s^{-1}$) is obtained for $\alpha = 4°$. Vorticity streets are again identified for both angles with higher vorticities.

3.2. *Turbulent kinetic energy and Reynolds stresses*

Turbulent kinetic energy for one data set at $\alpha = 4°$ is shown in Figure 10. As there are no significant differences among these ten sets, one is chosen for presentation.

Maximum kinetic energy is obtained in the vortex core center (x = -11.2552 mm and y = -1.6673 mm). This is very close to the data read for the previous realization presented in Figure 7(a), but coordinates are read from the PIV source file with a specified step. High turbulent kinetic energy values are also obtained along the vorticity sheet shown in velocity and vorticity distributions.

Similar distributions are obtained for all Reynolds stresses. Normal stress along the x-axis (Figure 11(a)) and shear stress in plane xy (Figure 11(b)) are shown below. Extremes are again obtained in the vortex core center and high values along the vorticity sheet.

3.3. *Turbulence structure in light of the invariant theory*

Anisotropy is a huge problem for turbulence modeling. Kolmogorov has formulated ideas about local-isotropic turbulence in his two hypotheses about similarity. The application of correlation theory, with the basic idea of a quantitative description of turbulence anisotropy, is used in the invariant theory of turbulence as a quantitative description of turbulence anisotropy. Lumley & Newman (1977) introduced the anisotropy tensor $\underline{\underline{A}} = a_{ij}\underline{e}_i\underline{e}_j$ as measure of turbulence as follows

$$\underline{\underline{A}} = -\left(\frac{1}{2\rho\rho}\underline{\underline{T}} + \frac{1}{3}\underline{\underline{I}}\right), a_{ij} = \frac{1}{2k}\overline{v_i v_j} - \frac{1}{3}\delta_{ij}\,, \tag{3.1}$$

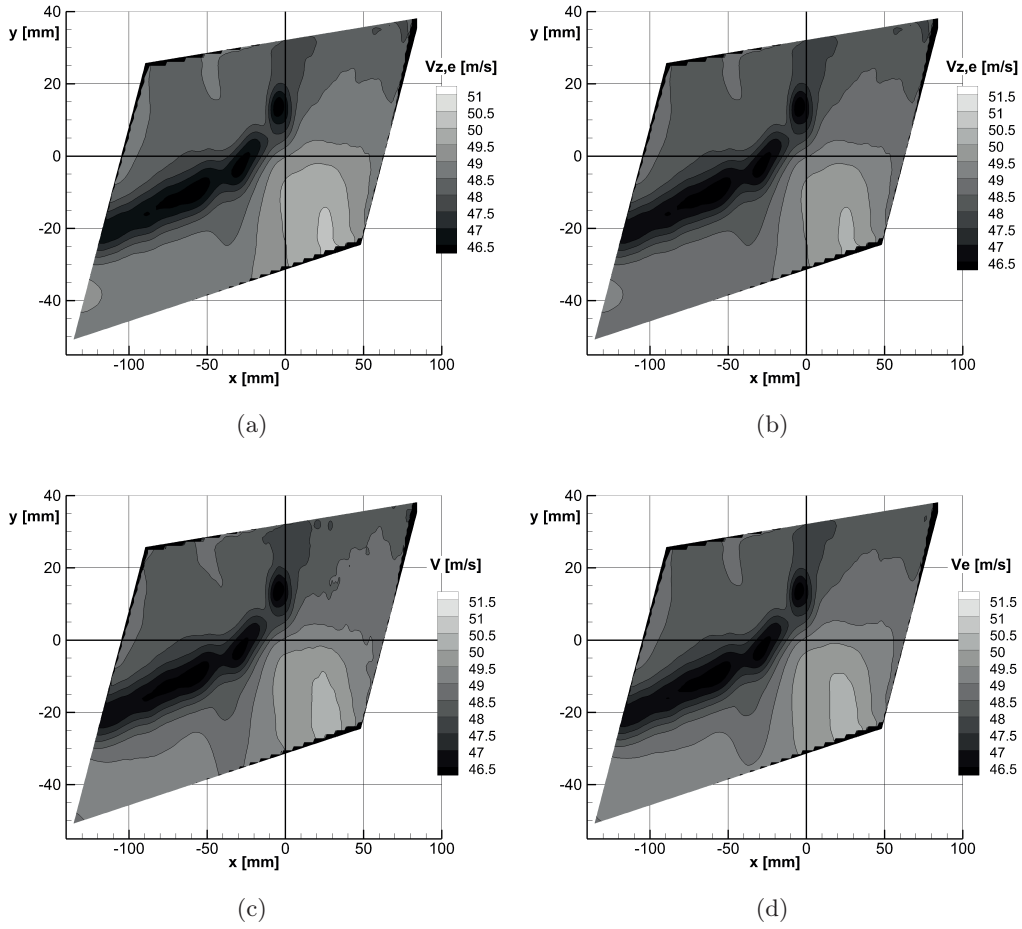

FIGURE 6. Velocity fields for $\alpha = 2°$: a) V_z, b) ensemble-averaged velocity V_z ($V_{z,e}$), c) averaged total velocity (V) for one data set, and d) ensemble-averaged total velocity (V_e).

where $\underline{\underline{T}}$- is a tensor of Reynolds stresses and $k = \frac{1}{2}(\overline{v_x^2} + \overline{v_y^2} + \overline{v_z^2}) = \frac{\overline{q^2}}{2}$ - turbulence kinetic energy. All components of tensor $\underline{\underline{A}}$ vanish in the case of isotropic turbulence $a_{ij} = 0$. Other states of turbulence anisotropy are analyzed on the basis of a_{ij} values, i.e., field of the second-order tensor $\underline{\underline{A}}$. Invariant theory, the mathematical tool based on the analysis of invariant anisotropy tensors, is practical for use in this sense. Čantrak (2012) applies invariant theory to the HSS PIV study of turbulent swirl flow behind the axial fan in a pipe. Scalar A presents the main eigenvalue of the tensor $\underline{\underline{A}}$ and satisfies equation $(\underline{\underline{A}} - A\underline{\underline{I}}) \cdot \underline{U} = 0$. Here, vector $\underline{U}$, which is a non-zero vector, is the main eigenvector of tensor $\underline{\underline{A}}$. A system of homogeneous linear equations is obtained if this expression is written in componential equation form in Cartesian coordinates $(a_{ij} - A\delta_{ij})U_j = 0$ for the vector components $\underline{U}$. It has non-zero solutions only for values A, which satisfy equation $\det ||a_{ij} - A\delta_{ij}|| = 0$. This equation can be written as

$$A^3 - I_a(\underline{\underline{A}})A^2 + II_a(\underline{\underline{A}})A - III_a(\underline{\underline{A}}) = 0\,, \tag{3.2}$$

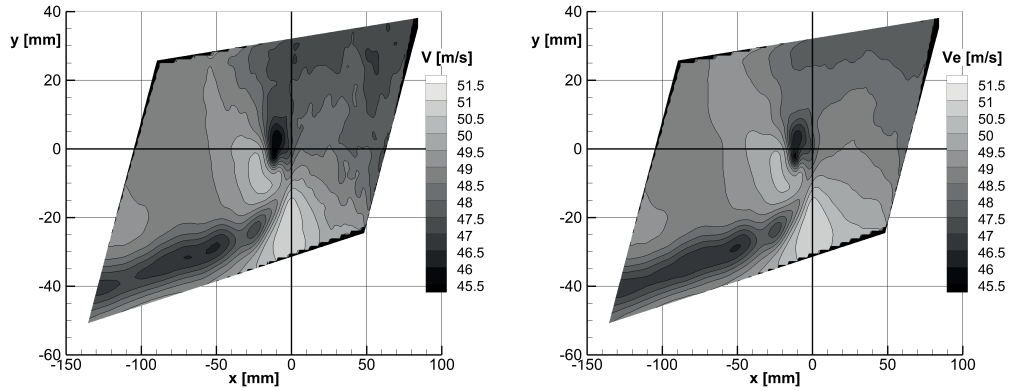

(a) (b)

FIGURE 7. Total velocity fields for $\alpha = 4°$: a) averaged total velocity (V) and b) ensemble-averaged total velocity (V_e).

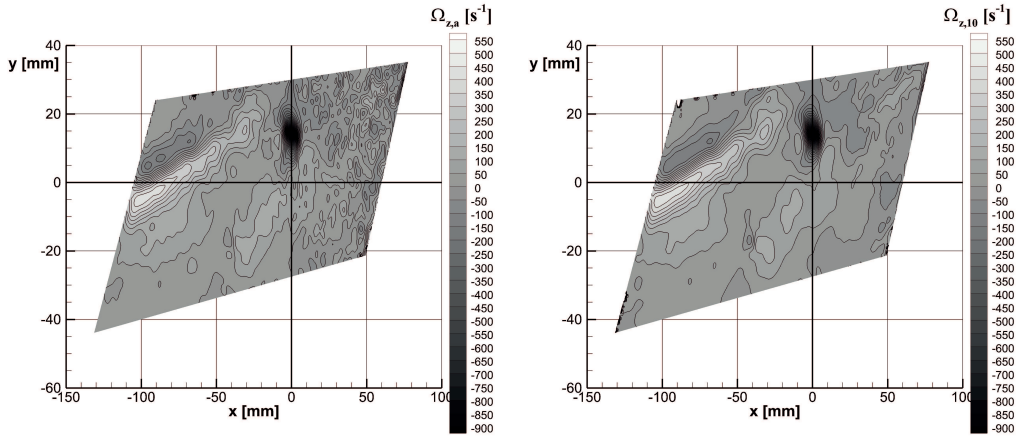

(a) (b)

FIGURE 8. Streamwise vorticity for $\alpha = 0°$: a) averaged vorticity for one data set ($\Omega_{z,a}$) and b) averaged vorticity for ten data sets ($\Omega_{z,10}$).

where I_a, II_a, and III_a are scalar functions of the components of the anisotropy tensor and present the first, second, and third invariants of the second-order tensor $\underline{\underline{A}}$

$$I_a = 0, II_a = -\frac{1}{2}a_{ij}a_{ji}, III_a = -\frac{1}{3}a_{ij}a_{ik}a_{jk} \, . \tag{3.3}$$

The study of turbulence anisotropy, which influences the dynamical properties of turbulence, is now reduced to the analysis of two independent values, i.e., two invariants of the anisotropy tensor defined with Eq. (3.3). In these experiments $\overline{v_i v_j}$ are measured. The scalar invariants II_a and III_a are determined on the basis of Eqs. (3.1) and (3.3). They are presented in the III_a-(-II_a) plane (Figure 12). All possible states of turbulence anisotropy belong to the curvilinear triangle area (012), the so-called Lumley triangle or

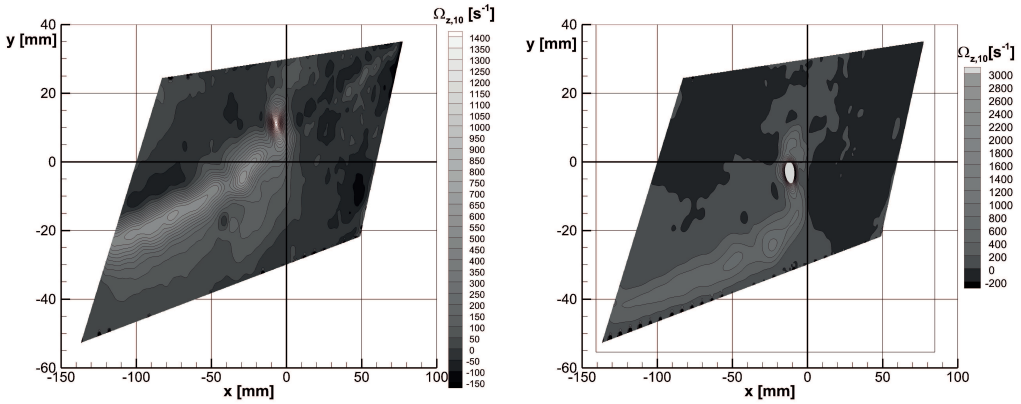

(a) (b)

FIGURE 9. Averaged streamwise vorticities for ten data sets each ($\Omega_{z,10}$) for α: a) 2° and b) 4°.

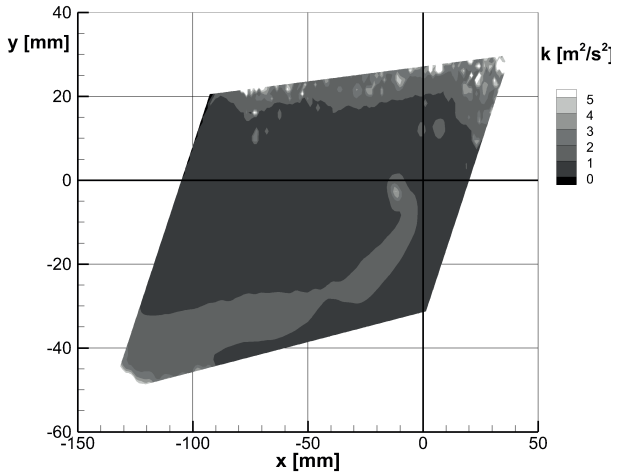

FIGURE 10. Turbulent kinetic energy for $\alpha = 4°$, experimental realization No. 4.

anisotropy invariant map. Lumley & Newman (1977) defined frontiers of the invariant map, which describe border states of turbulence, with the following equations

$$201 : -\mathrm{II_a} = \frac{3}{4}(4\,|\mathrm{III_a}|)^{2/3} + \frac{1}{9} \quad \text{and} \quad 21 : -\mathrm{II_a} = 3\mathrm{III_a} + \frac{1}{9}\,, \tag{3.4}$$

where 201 stands for axisymmetric turbulence, 20 stands for axisymmetric contraction and 01 for axisymmetric expansion, and 21 for two-component turbulence. Lumley triangle vertices 0, 1, and 2 (Figure 12(a)) correspond to turbulence boundary conditions. Point 0 corresponds to three-component isotropic turbulence, point 1 describes

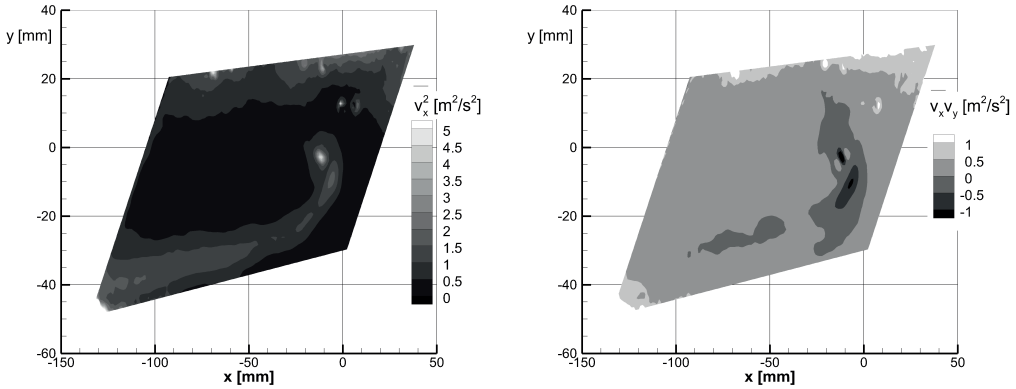

(a) (b)

FIGURE 11. Reynolds stresses for $\alpha = 4°$, experimental realization No. 4.: a) normal stress along the x-axis and b) shear stress in plane xy.

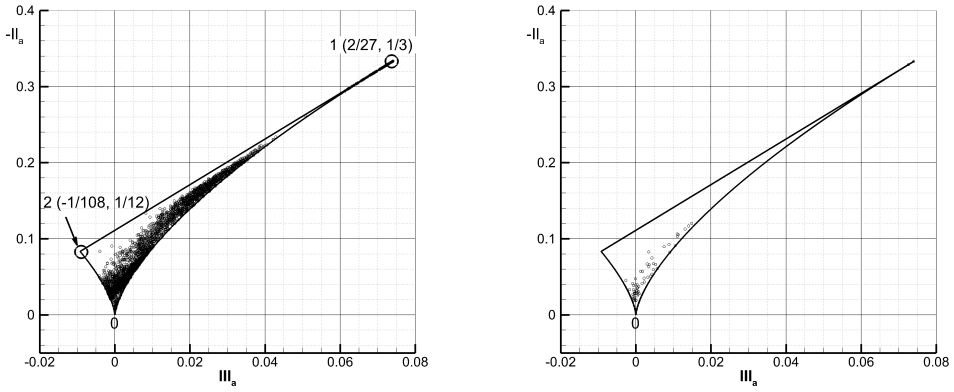

(a) (b)

FIGURE 12. Anisotropy invariant maps (Lumley triangles) for $\alpha = 4°$, experimental realization No. 4: a) all points and b) points along x = -11.2552 mm.

the boundary layer of one-component isotropic turbulence, while point 2 corresponds to two-component isotropic turbulence.

The second and third invariants are calculated for all measured points of $\alpha = 4°$ for one data set, i.e., experimental realization and are presented in Figure 12. The HSS PIV measuring technique can resolve fluid flow in this way in 1.044 s. All 10,075 points belong to the domain of invariant maps that include various physically possible turbulence states. Most of the points are distributed in the right part of the invariant map along the line 01 which characterizes the turbulence state of the axisymmetric expansion. Also, high point density is in the lower part of the invariant map, in the domain between curves 20 and 01 in the vicinity of point 0, which describes three-component isotropic turbulence.

Figure 12(b) shows 61 points along the direction x = -11.2552 mm where the vortex core is located. Most of the points are grouped in the vicinity of three-component isotropic turbulence. The point in the vortex core position x = -11.2552 mm and y = -1.6673 mm has coordinates in the invariant map ($III_a = 0.0022$ and $-II_a = 0.0481$). This is significantly close to the coordinates of the point 0 in the invariant map, which presents three-component isotropic turbulence. This resolves the nature of the wing tip vortex.

4. Conclusions

Investigation of the semi-span CRM has proved that wing tip vortices exist in the measurement plane three cords downstream of the end point of the wing tip profile for all three angles of attack (α).

Velocity intensities do not change significantly as a function of the angle of attack. Flow can be treated for all three angles of attack as statistically stationary.

Points of the total velocity minimum and streamwise vorticity maximum are obtained in the same points which denote vortex core coordinates for all angles of attack. The highest streamwise vorticity is obtained for $\alpha = 4^\circ$ and the lowest for $\alpha = 0^\circ$. It is also shown that the direction of vorticity is opposite for $\alpha = 0^\circ$ to that for the other two angles $\alpha = 2^\circ$ and $\alpha = 4^\circ$, which is consistent with a lifting wing. The vorticity sheet was also observed, and further investigation of turbulence statistics will be carried out in the future.

Turbulence kinetic energy, as well all Reynolds stresses, reach their maxima in the vortex core center. This is shown only for $\alpha = 4^\circ$.

All possible states of turbulence anisotropy of the flow studied for $\alpha = 4^\circ$ are investigated in the anisotropy invariant map. Almost all points are grouped in the right part of the Lumley triangle, close to the line 01 which describes the turbulence state of axisymmetric expansion. The highest number of points is in the vicinity of three-component isotropic turbulence, while the vortex core center has values close to this turbulence state.

Further HSS PIV and a pressure cobra probe measurements have already started. Experimental investigation on CRM will be continued with other measuring techniques such as PSP and FISF.

Additional HSS PIV measurements in planes one- and two tip-chords downstream of the wing tip are planned in order to document the streamwise evolution of the wing tip vortex. Flow measurements near the wing-fuselage junction are also planned.

Acknowledgments

Author Đorđe Čantrak conducted his research at the NASA Ames Fluid Mechanics Laboratory and Center for Turbulence Research at Stanford University as a Fulbright Visiting Scholar from April-June 2014. He expresses his gratitude to Prof. Dr. Peter Bradshaw, Prof. Dr. Parviz Moin, Director of the CTR, Dr. Rabindra Mehta, Experimetal Aero-Physics Branch Chief, Nasa Ames, and Dr. Srboljub Jović for their great support during his research. The authors owe special gratitude for support in the experimental work to all other FML members, especially Edward Schairer, Nettie Halcomb Roozeboom, Kurtis Long and Barry Porter. The authors also express their gratitude to Novica Z. Janković, University of Belgrade, Faculty of Mechanical Engineering, for his assistance in data analysis and text preparation. This CRM wind tunnel test was supported by the NASA Revolutionary Computational Aerosciences (RCA) project. Đorđe Čantrak also

expresses his gratitude to the Ministry of Education, Science and Technological Development, Republic of Serbia, Project No. TR 35046.

REFERENCES

Acheson, M. J. & Balakrishna, S. 2011 Effects of active sting damping on common research model data quality. *AIAA Paper 2011–878.*

Balakrishna, S. & Acheson, M. J. 2011 Analysis of nasa common research model dynamic data. *AIAA Paper 2011–1127.*

Bell, J. H. 2011 Pressure-sensitive paint measurements on the nasa common research model in the nasa 11-ft transonic wind tunnel. *AIAA Paper 2011–1128.*

Čantrak, Đ. S. 2012 *Analysis of the vortex core and turbulence structure behind axial fans in a straight pipe using PIV, LDA and HWA methods.* Ph.D. Thesis, University of Belgrade, Serbia.

Čantrak, Đ. S., Janković, N. Z. & Lečić, M. R. 2014 Laser insight into the turbulent swirl flow behind the axial flow fan. In *ASME Turbo Expo 2014 (GT2014-26563).*

Igarashi, H. *et al.* 2010 A stereoscopic piv study of a near-field wingtip vortex. *AIAA Paper 2010-1029.*

Illi, S. A. *et al.* 2013 Transonic tail buffet simulations for the common research model. *AIAA Paper 2013-2510.*

Lumley, J. L. & Newman, G. 1977 The return to isotropy of homogenous turbulence. *J Fluid Mech.* **82**, 161–168.

Rivers, M. B. & Dittberner, A. 2011 Experimental investigations of the nasa common research model in the nasa langley national transonic facility and nasa ames 11-ft transonic wind tunnel. *AIAA Paper 2011-1126.*

Rivers, M. B. & Hunter, C. A. 2012 Support system effects on the nasa common research model. *AIAA Paper 2012-0707.*

Rivers, M. B. *et al.* 2012 Further investigation of the support system effects and wing twist on the nasa common research model. *AIAA Paper 2012-3209.*

Schairer, E. T. *et al.* 2005 Predicting camera views for image-based measurements in wind tunnels. *AIAA Paper 2005-1349.*

Sohn, M. H. & Chang, J. W. 2012 Visualization and piv study of wing tip vortices for three different tip configurations. *Aerosp. Sci. Technol.* **16**, 40–46.

Spalart, P. R. 1998 Airplane trailing vortices. *Annu Rev Fluid Mech* **30**, 107–138.

Vassberg, J. C. *et al.* 2008 Development of a common research model for applied cfd validation studies. *AIAA Paper 2008-6919.*

Zilliac, G. G. *et al.* 2011 A comparison of the measured and computed skin friction distribution on the common research model. *AIAA Paper 2011-1129.*